

Soil Liquefaction–Induced Uplift of Underground Structures: Physical and Numerical Modeling

Siau Chen Chian¹; Kohji Tokimatsu, M.ASCE²; and Santana Phani Gopal Madabhushi³

Abstract: Underground structures located in liquefiable soil deposits are susceptible to floatation following a major earthquake event. Such failure phenomenon generally occurs when the soil liquefies and loses its shear resistance against the uplift force from the buoyancy of the underground structure. Numerical modeling accompanied with centrifuge experiments with shallow circular structures has been carried out to investigate the floatation failure at different buried depths of the structure. The influence of the magnitude of input sinusoidal earthquake shaking was also studied. Both numerical and experimental results showed matching uplift response of the structures and acceleration and pore-pressure measurements in the liquefied soil deposit. A higher uplift displacement of the structure was observed for shallower buried depth, thereby indicating the influence of overlying soil weight against floatation. Results also showed that the structures commenced floatation in the presence of high excess pore pressure, but they ceased when the earthquake shaking stopped. The higher rate of uplift in stronger earthquake shaking further substantiates the dependency of the uplift to the shaking amplitude. A constant rate of uplift of the structure was attained after the soil liquefied, hence postulating a possible limit to shear modulus degradation of the surrounding soil caused by soil-structure interaction. This is inferred by the lower excess pore-pressure generation near the structure. The displacement of liquefied soil around the displaced structure was also confirmed to resemble a global circular flow mechanism from the crown of the structure to its invert as observed in displacement vector plots obtained from numerical analysis and particle image velocimetry (PIV) in centrifuge tests. Further numerical analysis on the performance of buried sewer pipelines in Urayasu City, Chiba Prefecture following the 2011 Great East Japan Earthquake indicated high damage susceptibility of rigid pipelines in the liquefiable soil deposit. These consistencies with field observations clearly demonstrate and pave the prospects of applying numerical and/or experimental analyses for geotechnical problems associated with the floatation of underground structures in liquefiable soils. DOI: 10.1061/(ASCE)GT.1943-5606.0001159. This work is made available under the terms of the Creative Commons Attribution 4.0 International license, <http://creativecommons.org/licenses/by/4.0/>.

Author keywords: Earthquakes; Liquefaction; Underground structures; Numerical analysis; Centrifuge modeling; Pore pressures; Particle image velocimetry (PIV).

Introduction

Underground structures that serve as vital lifelines are susceptible to damage during a major earthquake. Although usually sheltered and protected by the overlying soil, underground structures such as large underground car parks, pipelines, and manholes can suffer significant uplift in liquefied soil as observed in numerous earthquake events, including the 2011 Great East Japan Earthquake (Tokimatsu et al. 2011). They are generally subjected to a buoyant force caused by their lower submerged unit weight than the surrounding soil. Under a static condition, the weight and shear strength of the overlying soil inhibits the floatation. In the event of liquefaction, the soil loses most of its shear strength, and the structure may float as a result. Existing major

lifelines built in earthquake-prone areas include the George Massey Highway Tunnel in Vancouver (Canada), San Francisco's Bay Area Rapid Transit (BART) Tunnel, Claremont Water Tunnels (California), and large-diameter natural gas pipelines in New Mexico, Japan, and Canada. Other seismically active regions are also planning or in the midst of constructing massive lengths of submersible tunnels in liquefiable soils, such as the Thessaloniki Highway Tunnel and Marmaray Rail Tunnel in Greece and Turkey, respectively. Each of these underground infrastructures carries thousands of commuters during peak hours and evidently poses extreme concerns to public safety in the event of a strong earthquake. Even a small amount of uplift can break longitudinal joints and lead to flooding.

The possibility of uplift of underground structures in a major earthquake was supported by several numerical and experimental analyses. Numerical analyses carried out by Yang et al. (2004) on the George Massey Tunnel and Sun et al. (2008) on the BART Tunnel showed significant floatation. These were substantiated with findings from centrifuge experiments carried out by Adalier et al. (2003) and Chou et al. (2011), who observed a significant amount of sand displacing toward the invert of the uplifted underground structure when simulating conditions of the George Massey Tunnel and BART Tunnel, respectively. The uplift was observed to be affected by both the input earthquake shaking intensity and the generation of excess pore pressure. Sasaki et al. (1999) also noted that the uplift displacement of pipes was significant when input acceleration was large or when the density of sand was low in their centrifuge tests. In the case of manholes, Tobita et al. (2012) postulated that the primary cause of uplift is the reduction of the effective

¹Assistant Professor, Dept. of Civil and Environmental Engineering, National Univ. of Singapore, Engineering Dr. 2, E1A-07-03, Singapore 117576 (corresponding author). E-mail: sc.chian@nus.edu.sg

²Professor, Dept. of Architecture and Building Engineering, Tokyo Institute of Technology, 2-12-1 O-okayama, Meguro-ku, Tokyo 152-8550, Japan. E-mail: kohji@o.cc.titech.ac.jp

³Professor, Dept. of Engineering, Univ. of Cambridge, Schofield Centre, Madingley Rd., High Cross, Cambridge CB3 0EL, U.K. E-mail: mspg1@eng.cam.ac.uk

Note. This manuscript was submitted on August 12, 2013; approved on June 4, 2014; published online on July 11, 2014. Discussion period open until December 11, 2014; separate discussions must be submitted for individual papers. This paper is part of the *Journal of Geotechnical and Geoenvironmental Engineering*, © ASCE, ISSN 1090-0241/04014057 (18)/\$25.00.

confining stress near the bottom of a manhole caused by strong shaking. The liquefied soil flow toward the bottom of the manhole was caused by the anisotropic stress state, which causes uplift. Given the enormous risk present should one of these vital lifelines fail in a major earthquake, there exists a need to conduct in-depth research to better understand and mitigate such seismic megarisk, which could bring cities to a standstill in a major earthquake event. At present, geotechnical studies carried out on the floatation of underground structures in liquefiable soil are limited as previously pointed out by Ling et al. (2003). The factor of safety against floatation adapted from Koseki et al. (1997) was later developed further and verified with centrifuge experiments for pipes (Ling et al. 2003) and manholes (Tobita et al. 2012). However, such factor of safety procedures only provide the triggering condition of uplift and fall short of predicting the final uplift displacement of underground structures (Tobita et al. 2012). Numerical analysis was successfully conducted to simulate the dynamic response of the soil and pipe up to the stage of liquefaction (Ling et al. 2008). However, large soil-strain simulation during the postliquefaction phase remains a challenge to date with conventional numerical methods.

The aforementioned studies provide useful information on the uplift displacement of underground structures in liquefiable soils. However, knowledge gaps persist, particularly in the prediction of uplift displacement of underground structures and simulation of postliquefaction response of the soil in numerical analysis. This paper presents a combination of numerical and experimental investigations of circular buried structures in homogeneous liquefiable soil to better understand the fundamentals of uplift response of underground structures in general. The commencement and cessation of the uplift are discussed in relation with the input acceleration and excess pore pressure generated in the soil deposit. The soil deformation around the uplifted structure was also investigated to provide a more holistic understanding of the uplift mechanism of buoyant underground structures. Further analysis on the performance of underground sewer pipes in Urayasu City, Chiba Prefecture near Tokyo subjected to the ground motion following the 2011 Great East Japan Earthquake showed significant uplift displacement in liquefiable soil deposit, which is in agreement with the damage of these pipelines observed in the field.

A simplified mechanism for the floatation of a circular underground structure is portrayed in Fig. 1. The buoyant force of the structure (F_B) is governed by the Archimedes principle. This buoyancy force is equivalent to the displaced volume of water

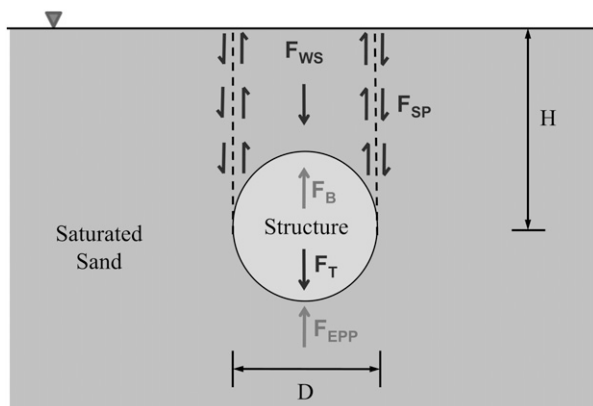


Fig. 1. Forces acting on a pipe in liquefied soil

multiplied by the unit weight of water ($\gamma_w = 9.81 \text{ kN/m}^3$) where the structure is immersed. The weight of the structure (F_T) refers to the force caused by the mass of the structure under gravity. The weight of the overlying soil (F_{WS}) considers the effective surcharge of the soil acting on the structure, whereas the shear contribution (F_{SP}) is proportional to the shear strength of the soil and buried depth of the structure.

The resistance forces inhibiting the uplift force because of buoyancy (F_B) are provided by the weight of the structure (F_T), weight of the overlying soil (F_{WS}), and shear resistance developed in the soil (F_{SP}). However, in the event of soil liquefaction during an earthquake, the shear contribution could be reduced significantly. In addition, the excess pore pressure generated near the invert of the structure (F_{EPP}) can also contribute to the uplift force acting on the structure. When there is a positive net uplift force (F_{NET}) as shown in Eq. (1), the structure may float as a result

$$F_{NET} = (F_B + F_{EPP}) - (F_T + F_{SP} + F_{WS}) \quad (1)$$

Centrifuge Modeling

Soil is a highly nonlinear material and is therefore essential to replicate identical stress and strain conditions in laboratory tests as in the prototype scale. Geotechnical centrifuge modeling achieves these conditions with the use of high centrifugal acceleration to scale up the model. A scaled model is made to correspond with the prototype at the predetermined centrifuge g level. As a result, a 1: N model experiences the same stress-strain condition as the prototype when subjected to a centrifugal acceleration of a $N \times g$ level (Schofield 1980). Table 1 shows a set of scaling laws to interpret other centrifuge testing parameters at a prototype scale.

It is recognized in physical modeling that there is a disparity between the scaling law for the time for diffusion processes (e.g., consolidation given by $1/N^2$) and dynamic events (given by $1/N$). This disparity is resolved by using a pore fluid of viscosity that is N times greater than water (normal pore fluid). By increasing the viscosity of the pore fluid, both the rate of excess pore-pressure generation (caused by earthquake loading) and rate of dissipation (caused by soil consolidation) are matched. This is a widely

Table 1. Centrifuge Scaling Laws (Data from Schofield 1981)

Parameter	Model/prototype	Units
General scaling laws (slow events)		
Length	$1/N$	m
Area	$1/N^2$	m^2
Volume	$1/N^3$	m^3
Mass	$1/N^3$	$\text{N s}^2/\text{m}$
Stress	1	N/m^2
Strain	1	—
Force	$1/N^2$	N
Seepage velocity	$1/N$	m/s
Time (consolidation)	$1/N^2$	s
Dynamic events		
Time (dynamic)	$1/N$	s
Frequency	N	1/s
Displacement	$1/N$	m
Velocity	1	m/s
Acceleration/acceleration caused by gravity	N	m/s^2

established procedure used by dynamic centrifuge modelers globally (Stewart et al. 1998).

Centrifuge tests to investigate the uplift of the structure in liquefied soil were conducted on the 10-m-diameter beam centrifuge at

Cambridge University. Specific design and operation of the beam centrifuge are provided by Schofield (1980). The stored angular momentum (SAM) earthquake actuator devised by Madabhushi et al. (1998) was used to apply near-sinusoidal earthquake motions to the centrifuge model.

The model boxes used in the centrifuge tests were the equivalent shear beam (ESB) box and window box. The design and performance compliance of the ESB box are described by Zeng and Schofield (1996) and Teymur (2002). The window box is made up of an aluminum container with a Perspex window panel for viewing during testing. Images of the soil and buried structure can be easily captured through the Perspex with a high-speed camera (Chian and Madabhushi 2010; Cilingir and Madabhushi 2011). To reduce the reflection of incident stress waves caused by the rigid boundary of the container, 25 mm of moldable Duxseal (JM Clipper Corporation, Nacogdoches, Texas) were placed on the sides of the container to reduce reflecting incident stress waves by at least 65% (Steedman and Madabhushi 1991) and achieve semiinfinite boundaries given

Table 2. Material Properties of Hostun Sand

Properties	Hostun sand
ϕ_{crit} (degrees)	33 ^a
D_{10} (mm)	0.209
D_{50} (mm)	0.335
e_{min}	0.555 ^a
e_{max}	1.01 ^a
G_s	2.65 ^a
K ($\times 10^{-3}$ m/s)	1 ^b

^aData from Mitrani (2006).

^bData from Haigh et al. (2012).

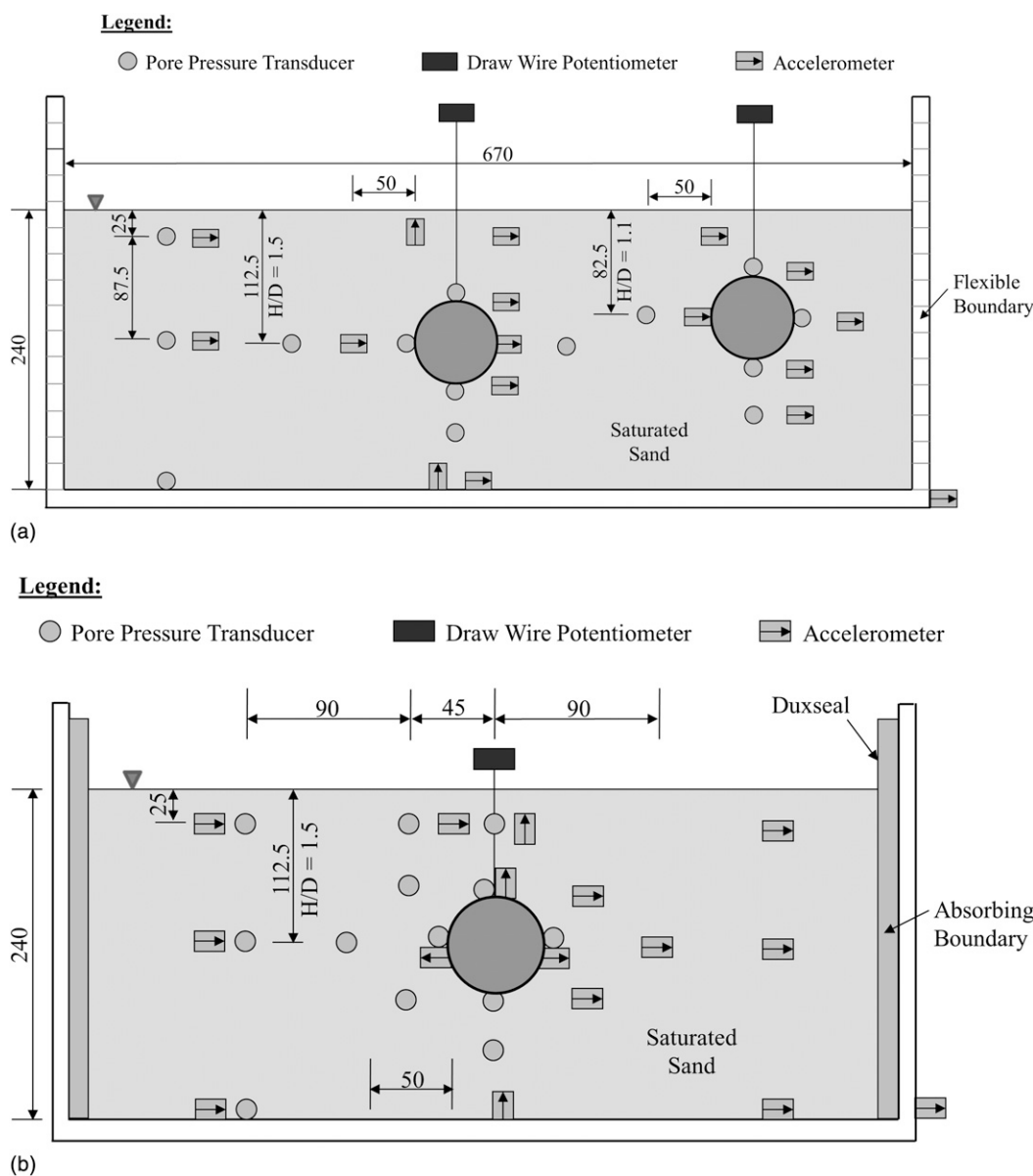
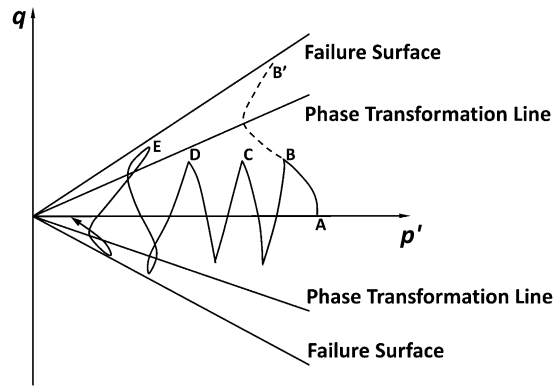


Fig. 2. Typical centrifuge model layouts: (a) in ESB box for Tests 1.1D_0.22g and 1.5D_0.22g; (b) in window box for Test 1.5D_0.22g

Table 3. Centrifuge Test Configurations

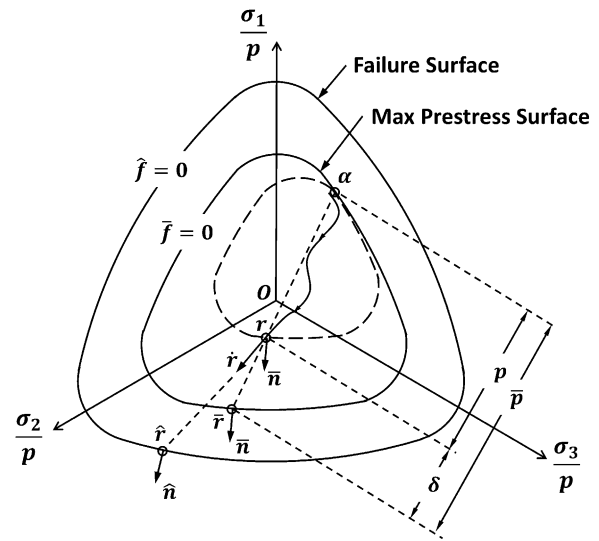
Test identification	Peak input acceleration (g)	Buried depth to axis/diameter	Type of strong box
1.1D_0.22g	0.22	1.1	ESB box
1.5D_0.22g	0.22	1.5	ESB box
1.5D_0.10g	0.10	1.5	Window box

**Fig. 3.** Effective stress paths under monotonic (Path ABB') and cyclic undrained triaxial loading (Path $ABCDE$) (adapted from Wang et al. 1990, © ASCE)

the compressibility properties (Cheney et al. 1988). The Duxseal remained stable and did not show any unusual deformations after each centrifuge test. This substantiates optimum molding of the Duxseal to achieve the desired boundary condition, similar to the ESB box.

An automatic sand pourer was used to prepare the loose sand model. It relied on the concept of sand pluviation by gravity. The sand was pluviated dry; therefore, the relative density could be closely monitored. Each set of pours with sand thickness of approximately 15 mm was checked for uniformity of relative density based on the change in mass of the sand and approximate volume of sand deposited into the model box. Design charts from Chian et al. (2010) based on an extensive database of relative density with varying parameters of the automatic sand pourer apparatus were referred to provide a reliable estimate of the expected thickness of sand and relative density of the pour. These design charts showed a general trend that an increase in drop height and/or reduction in outflow nozzle diameter of the pour at a given velocity of travel of the hopper would yield a higher relative density of the sand deposited. Hostun sand of relative density (45%) was prepared in the models. The material properties are described in Table 2. In the midst of sand pouring, instruments were placed at specific predetermined depths and locations based on the configuration layouts shown in Fig. 2. The instrumentation used in these models consists of accelerometers, pore-pressure transducers, and draw-wire potentiometers. Identical circular hollow structures with closed ends were buried at a depth of 1.1 and 1.5 times its diameter in the sand to ascertain their difference in uplift response with respect to their depth. Securing supports were also put in place to avoid any accidental movement of the structure prior to centrifuge testing.

The model was subsequently saturated under vacuum while fluid flows through four inlet pipes at the base of the model box. The saturation front progresses upward to the soil surface, which reduces the presence of entrapped air in the void by driving the air out of the model as pore fluid fills the void in the soil. The in-house designed Cam-Sat system monitors the fluid flow rate and adjusts the optimum pressure difference between the fluid feeding tank and model

**Fig. 4.** Illustration of model mechanism in deviatoric stress ratio space (reprinted from Wang et al. 1990, © ASCE)**Table 4.** Soil Properties Used in Numerical Analyses

Parameter	Values
Dry density (ρ_d)	1,450 kg/m ³
Saturated density (ρ_{sat})	1,860 kg/m ³
Bulk modulus (K)	1.5×10^7 Pa
Shear modulus (G)	5.5×10^6 Pa
Internal friction angle (ϕ)	33°
Cohesion (c)	0 Pa
Initial void ratio (e)	0.8
Permeability	1×10^{-3} m/s
Small elastic shear modulus coefficient (G_0)	150
Shear modulus reduction coefficient (h_r)	0.7
Effective stress coefficient (k_r)	0.06
Cyclic pore-pressure coefficient (d)	2.0

box to ensure consistent and relatively low upward hydraulic gradient during saturation (Stringer and Madabhushi 2009).

Centrifuge g level of 66.7g was conducted to scale the model structure of 75 mm in diameter to the prototype scale of 5 m in diameter. The mass of the structure, including attached instruments at the prototype scale, was about 6 t (specific gravity, G_s of 0.3). Near-sinusoidal earthquake shaking of about 27 s at 0.75 Hz at the prototype scale was applied at the base of the centrifuge models. A summary of the test configurations is shown in Table 3.

Numerical Modeling

Numerical analysis was carried out using *Fast Lagrangian Analysis of Continua (FLAC) 7*, a finite-difference program code developed by Itasca Consulting Group as a general two-dimensional analysis of geotechnical/geological media for computing large deformations. The program has been widely used in several geotechnical problems, such as slope stability, embankment, deep excavation, and tunneling. The program is also capable of simulating yielding and flow of materials at a large strain with low computation demand given its Lagrangian calculation scheme and mixed-discretization zoning technique without matrices formed (FLAC).

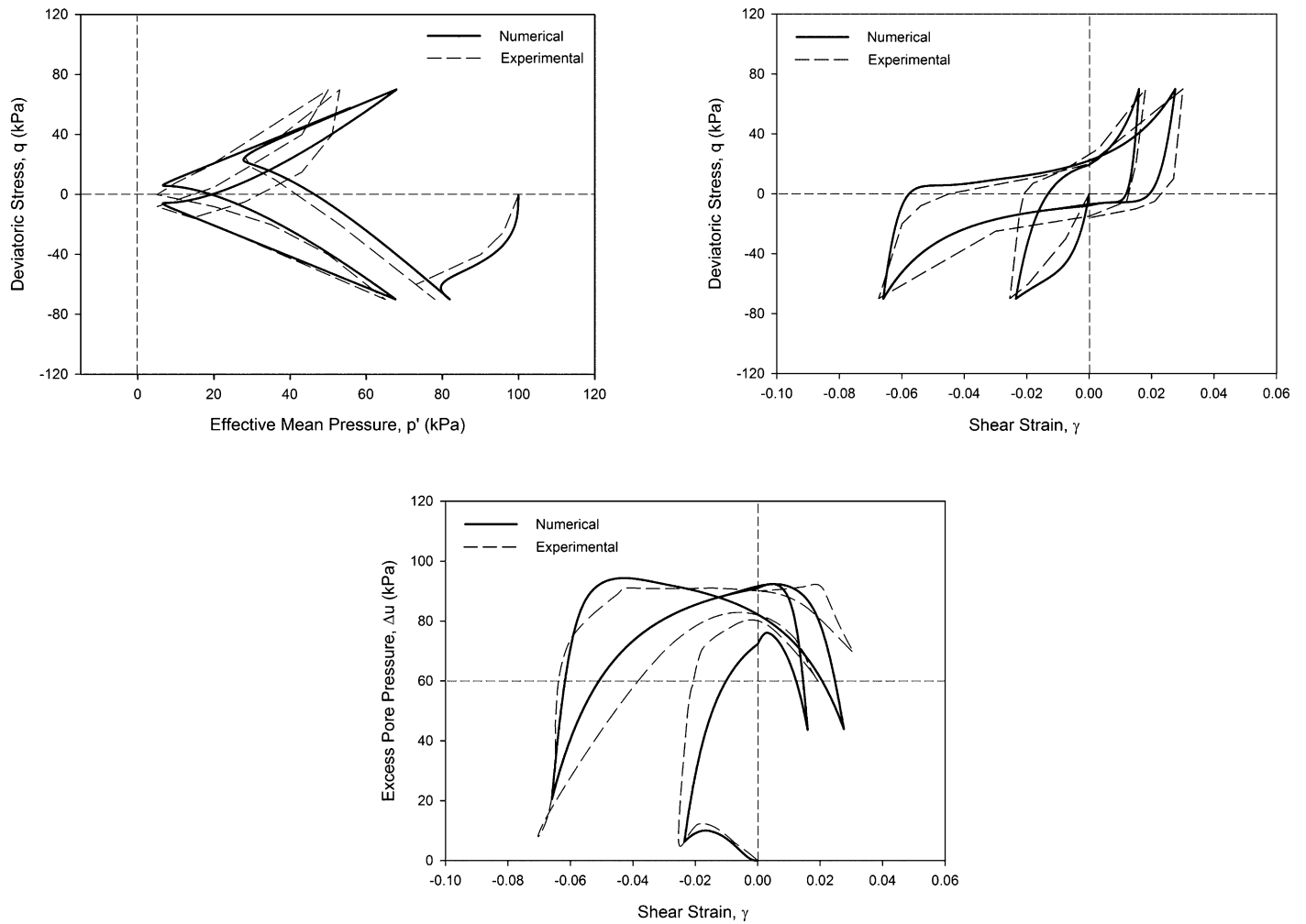


Fig. 5. Model simulation of cyclic test for Hostun sand (experimental data from Bouferra et al. 2007)

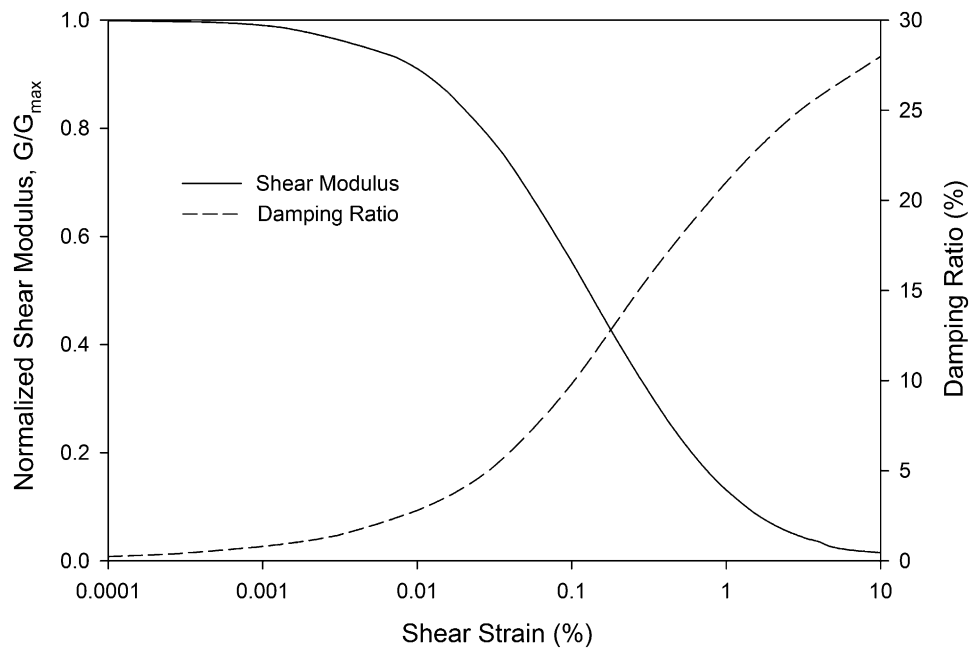


Fig. 6. Shear modulus degradation and corresponding damping curves ($G_{max} = 5.5 \times 10^3$ kPa, $\tau_m = 7.5$ kPa)

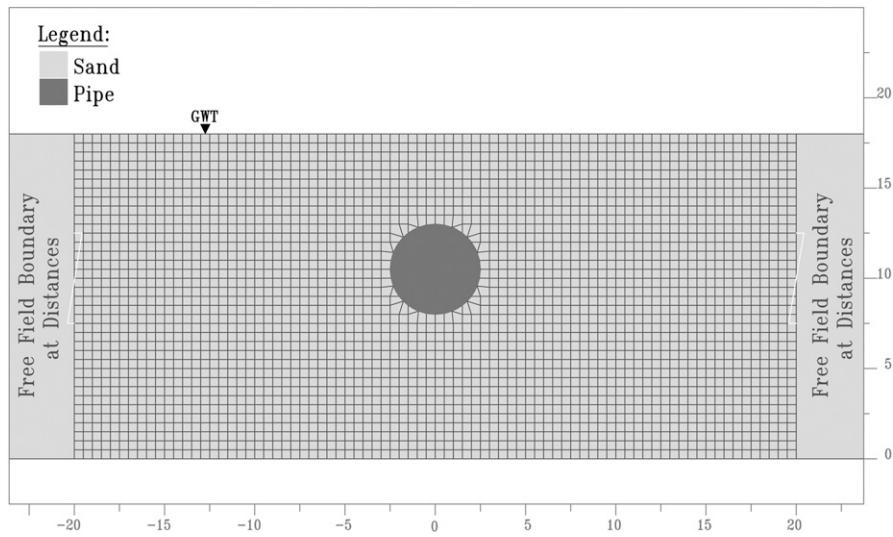


Fig. 7. Typical numerical layout for tunnel buried depth of $H = 1.5D$ (dimensions in meters)

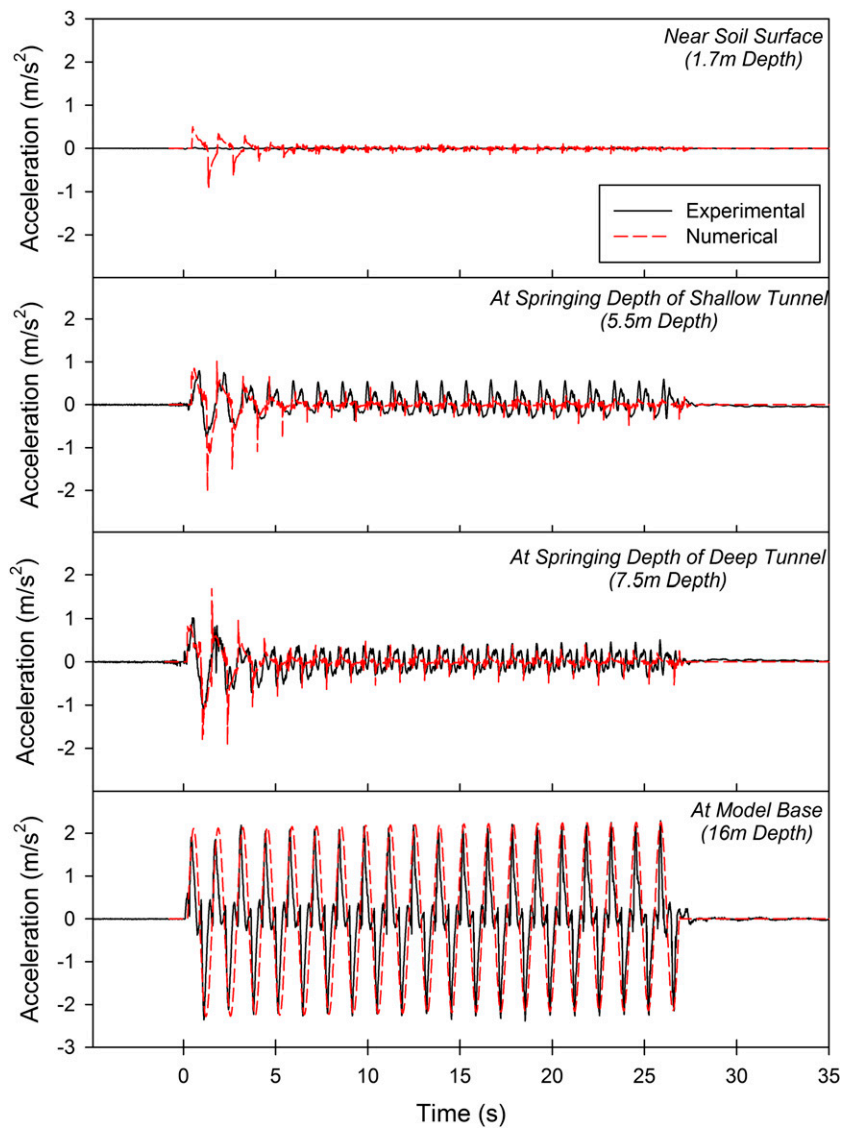


Fig. 8. Typical far-field acceleration time histories, Test 1.1D_0.22g

A user-defined continuum soil model, the Wang model (Wang et al. 1990), was applied in the analysis to simulate soil liquefaction properties and response. The Wang model is a nonlinear, fully coupled bounding surface plasticity constitutive model for sand, which is specifically formulated to capture the contraction and dilation induced by cyclic shear stresses. Fig. 3 shows the failure surface and phase transformation line considered in the model. In Fig. 3, q' and p' refer to the deviatoric stress and effective mean stress, respectively. Four cycles of undrained triaxial loading is demonstrated as an example where p' reduces to near zero and the soil dilates after crossing the phase transformation line. This is in contrast with the effective stress path ABB' under monotonic undrained loading as indicated with a discontinuous line.

Further depiction of the concept of the Wang model can be illustrated with the model mechanism in the deviatoric stress ratio space, with a loading surface resembling a cone with its apex at the origin $\bar{f} = 0$ and $\hat{f} = 0$, representing the maximum prestress memory surface and a fixed failure surface, respectively, as shown in Fig. 4. During a reversal loading from point α to the current stress r , a new

loading surface as shown with a discontinuous line homologous to $\bar{f} = 0$ is created. If r lies on the $\bar{f} = 0$ surface, the new loading surface becomes identical to the $\bar{f} = 0$ surface. Two image stress points, \bar{r} and \hat{r} are defined from the stress ratio r as shown in Fig. 4. Point \bar{r} is located along the $\bar{f} = 0$ surface and obtained from the radial projection of the line passing through α and r . Point \hat{r} is obtained from the extension of the r direction onto the $\bar{f} = 0$ surface. The unit vectors to $\bar{f} = 0$ and $\hat{f} = 0$ are defined as \bar{n} and \hat{n} , which are the basis to the model's hypoplastic nature. The plastic moduli are functions of the scalar distances δ , p , and \bar{p} as shown in Fig. 4. This concept has been widely studied (Hashiguchi and Ueno 1977; Dafalias and Popov 1977; Mroz and Zienkiewicz 1984). Further details on the formulation of the model are provided by Wang et al. (1990).

The soil properties used in the analysis of the uplift of structures to represent the soil condition in the centrifuge tests are presented in Table 4. The constitutive model-dependent parameters, namely the modulus coefficient defining the small-strain elastic shear modulus (G_0), reduction of the shear modulus with increasing strain amplitude (h_r), and blow count related k_r and d were calibrated to produce similar

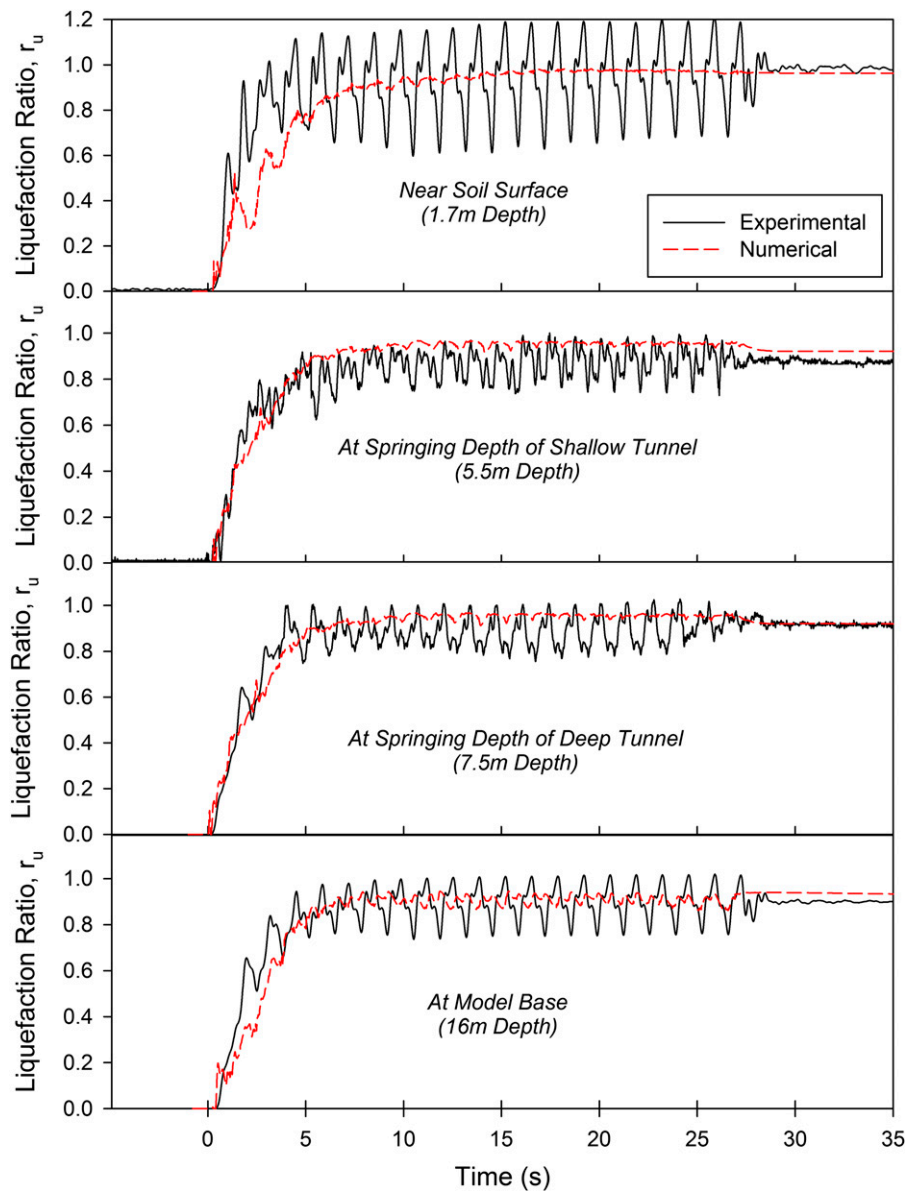


Fig. 9. Typical far-field liquefaction ratio time histories, Test 1.1D_0.22g

contractive and dilative responses as typical cyclic laboratory tests of loose saturated Hostun sand as shown in Fig. 5, which were similar to those used in the centrifuge modeling. The stress-controlled undrained cyclic triaxial test on the saturated Hostun sand specimen prepared to a relative density of about 50% was subjected to a cell pressure (σ_3) of 100 kPa and cyclic deviatoric stress amplitude (q) of 70 kPa to failure (Bouferra et al. 2007). Fig. 6 shows the shear modulus degradation and corresponding damping curves used in the analysis.

The mass of the model structure in the numerical modeling was calibrated to have a similar overall unit weight ($G_s = 0.3$) as in the centrifuge tests. Fig. 7 shows the layout of the numerical model. The frictional interface between the structure and soil was taken to be a friction angle of 21.8° ($\mu = 0.4$). The problem was taken as a plane strain, and the structure was assumed as rigid as in the centrifuge testing. The seismic input can be represented by plane waves propagating upward through the soil. Hence, the boundary conditions at the sides of the model must account for the free-field condition. Given the application of only a simple one-dimensional (1D) input wave, the boundary conditions may be addressed by two methods: (1) applying a 1D free-field calculation in parallel with the main grid analysis, or (2) constructing a wide model so that the vertical boundaries are placed at distances sufficient to minimize wave reflections and achieve free-field conditions. Both methods were adapted in the numerical model. The former allowed a free field with absorbing capability to be applied to the vertical boundaries, whereas the latter further ensured wave reflections were negligible and provided stability to the model during earthquake shaking.

Far-Field Measurements of Acceleration and Pore Pressure in Liquefiable Soil

In a liquefying soil deposit, it is expected that excess pore-water pressure is generated accompanied with attenuation of seismic waves. With the build-up of excess pore-water pressure, the soil's shear strength is reduced, which hampers effective propagation of shear waves to the soil surface. This is supported by Figs. 8 and 9, which show the far-field acceleration and liquefaction ratio time history plots obtained, respectively, from the numerical analysis and experimental test results. The liquefaction ratio, r_u , is defined as the change in pore pressure divided by the initial vertical effective stress of the soil ($r_u = \Delta u / \sigma'_v$). Based on the numerical and experimental results, it is apparent that both the generation of excess pore pressure and propagation of seismic waves from the model base to the soil surface were generally similar at all depths of the saturated sand model. Some discrepancies, however, exist between the experimental and numerical analyses. Strong dilative response of the soil prior to liquefaction and incidental noise in the form of sharp spikes derived from a higher sampling rate were observed in the acceleration time histories produced by the numerical model when compared with the experimental data. However, at full liquefaction, the amount of shear-induced dilation in each cycle was somewhat underestimated in the numerical analysis as inferred by the lower peak-to-peak values. Such observations were also present in analysis performed with other liquefaction constitutive models (Byrne et al. 2004), which indicate possible setup differences. For example, minor differences in the boundary condition

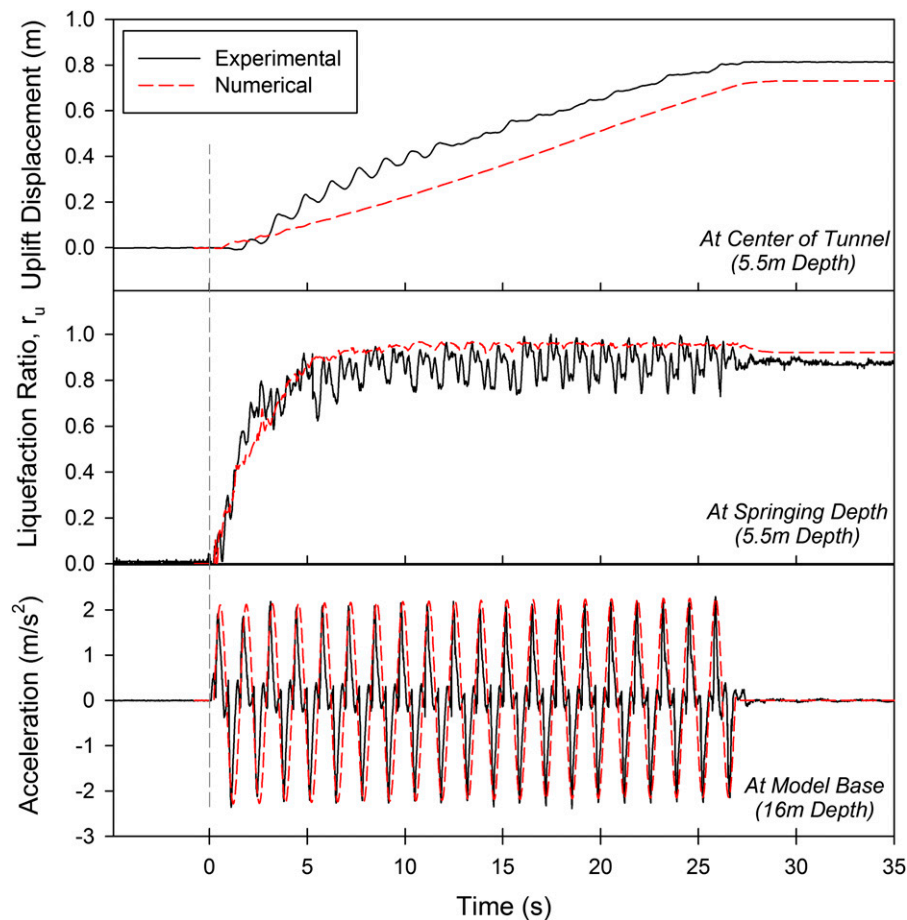


Fig. 10. Uplift displacement, far-field liquefaction ratio, and input acceleration time histories, Test 1.1D_0.22g

may lead to such discrepancies between the numerical and experimental analyses. This is portrayed by the more rapid liquefaction and attenuation of acceleration near the soil surface in the centrifuge tests compared with the numerical simulations. The imperfect sinusoidal motion of the shaking table in the centrifuge tests also led to the additional cyclic amplitudes in the experimental data, which are not present in the smooth sinusoidal shaking in the numerical simulation. In addition, some vertical shaking caused by the jaw configuration of the shaking table in the centrifuge may also have caused cyclic changes to the vertical stress of the soil and hence larger peak-to-peak amplitude in the excess pore-pressure time histories. Nevertheless, the similarities in the overall trend of acceleration and excess pore-pressure time histories are encouraging for such early application of the numerical analysis, which is capable of both simulating postearthquake response and estimating uplift of underground structures reasonably.

Uplift Displacement of Buoyant Structures in Liquefiable Soil

Based on the theoretical floatation mechanism previously discussed in Eq. (1), it is suggested that a buoyant structure may float when the soil's shear strength from its interparticle frictional contact is reduced with the generation of excess pore-water pressure. Floatation of the structure is hence assumed to be initiated as a result of build-up of high pore-water pressure. This is substantiated with the commencement of the uplift as observed in the numerical analysis and

centrifuge test in Fig. 10. Excess pore pressure was generated almost instantaneously with the application of strong shaking followed by the uplift of the structure. Both the numerical analysis and experimental results also showed that the floatation generally took place only during the earthquake loading and ceased when the earthquake stopped, despite retaining high excess pore pressures. This infers that the uplift of the structure in liquefied soil did not behave as a buoyant structure in viscous fluid, which would otherwise show continual uplift of the structure after shaking. Clearly, these findings portrayed that the uplift response was highly influenced by the earthquake loading apart from the presence of high excess pore pressure alone. A constant rate of uplift was also attained after the soil had fully liquefied, inferring a possible limit to the shear modulus degradation of the overlying soil caused by the soil-structure interaction. In view of the matching far-field response of the soil in Figs. 8 and 9 accompanied with a similar trend and magnitude of uplift displacement measurements of the structure in Fig. 10, it is evident that the numerical analysis is capable of producing a good general depiction of the response of the liquefying soil under earthquake shaking in the centrifuge test conducted.

Further investigations between numerical and experimental results showed that the uplift response of the structure obtained from the numerical analysis was more gradual compared with the centrifuge test results portrayed in Fig. 10. Despite achieving a fairly similar magnitude of excess pore pressure at the springing depth (i.e., at depth H as illustrated in Fig. 1) of the structure, it appeared that the structure in the centrifuge test was experiencing some resistance to uplift at the early stage of the floatation as observed in

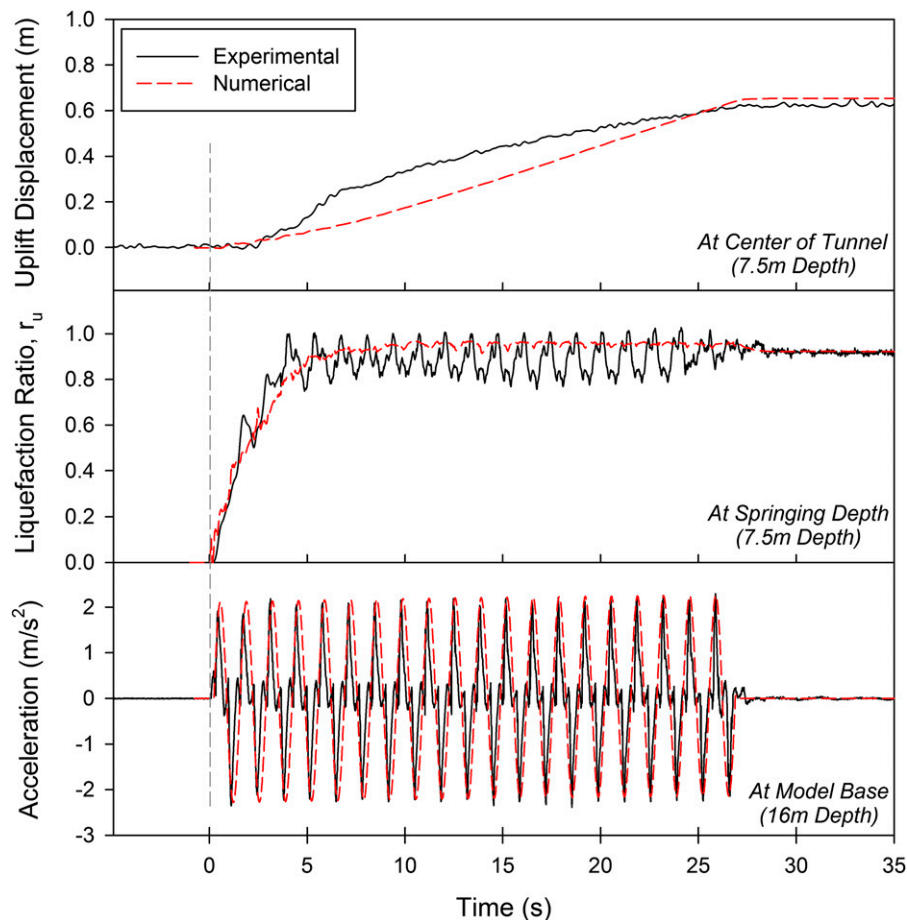


Fig. 11. Uplift displacement, far-field liquefaction ratio, and input acceleration time histories, Test 1.5D_0.22g

Fig. 10. The commencement of the structure uplift in the centrifuge test was lagging behind the numerical analysis. This was followed with an abrupt increase in the rate of uplift after about two to three cycles of shaking. The cyclic uplift response as observed in the uplift displacement plot also implied that the structure was experiencing significant fluctuation of force acting on it. The rate of uplift thereafter decreased slightly and attained a near constant value until the end of the earthquake shaking. In contrast, the numerical analysis results showed a gradual increase in rate of uplift with an increase in the liquefaction ratio during the first three cycles of shaking before attaining a constant uplift rate when the liquefaction ratio was near 1.0. Similar observations were evident in the case of the deeper buried structure ($H/D = 1.5$) as shown in Fig. 11. Although higher peak-to-peak excess pore pressures were generated in the centrifuge tests as inferred from the far-field liquefaction ratio plots in Fig. 9, this does not fully explain the difference in the early uplift response of the structure between the two types of modeling. Nevertheless, these differences between the numerical analysis and centrifuge test results did not hamper the satisfactory comparison of the final uplift displacement measurements of the structure. This is substantiated with another centrifuge test ($1.5D_{0.10g}$), with a lower input peak acceleration of $0.1g$ as shown in Fig. 12.

Numerical and experimental results from the three tests showed an increase in uplift displacement of the structure with higher input acceleration and shallower depth, which was anticipated. Higher input acceleration produces greater uplift displacement of the structure, which indicates the strong influence of the earthquake's shaking amplitude on the uplift response of the structure during the

earthquake and cessation of the uplift as previously mentioned. Shallower embedment of the structure provides lower resistance against uplift because of the shorter length of the shear planes (lower F_{SP} in Fig. 1) and lower effective weight of overlying soil (F_{WS}) suppressing the uplift, respectively.

Pore Pressure around Buoyant Structures in Liquefiable Soil

Given the strong influence of excess pore-pressure generation on the uplift of underground structures, it is essential that further investigation be directed toward the pore-pressure readings near the structure to assess the influence of the soil-structure interaction. This may also address some of the earlier discrepancies of the uplift response of the structure between the numerical analysis and centrifuge results at the early stage of the earthquake shaking where far-field pore pressures did not reflect any differences. In the midst of floatation, it is expected that excess pore-pressure transducers attached to the floating structure would register a lower value given the reduction in depth of the soil. These excess pore-pressure readings were therefore adjusted with the corresponding uplift displacement time history to produce a consistent benchmark soil depth prior to shaking. The adjustment involves adding the change in vertical effective stress caused by the reduction in depth (i.e., $\Delta_{\text{uplift}} \times \gamma'$) to the raw excess pore-pressure data as demonstrated in Fig. 13. This is so that comparisons could be made between the near and far field and structures with different uplift displacements

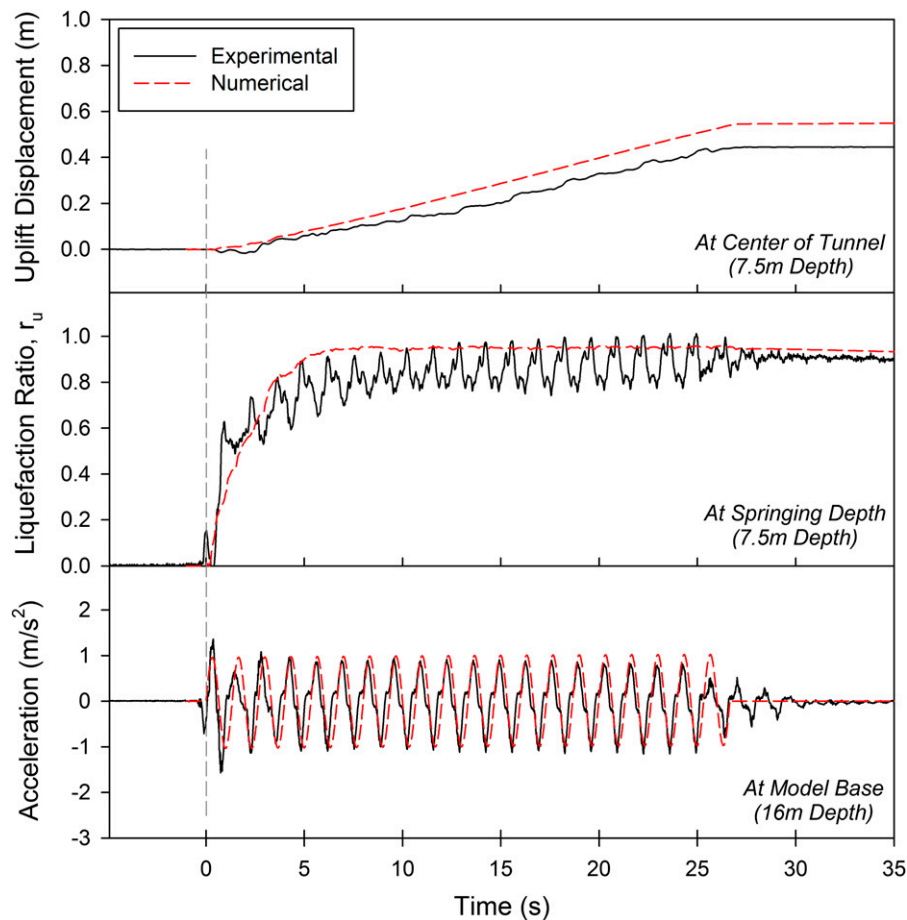


Fig. 12. Uplift displacement, far-field liquefaction ratio, and input acceleration time histories, Test $1.5D_{0.10g}$

objectively. Figs. 14 and 15 show the excess pore-pressure time histories at the invert, springing, and crown of the structures during the shaking. Despite making the necessary adjustment, most of these readings were significantly lower than those at the far field as shown in Fig. 16. This indicates the likelihood of influence from the soil-structure interaction. A lower excess pore pressure infers that a portion of the soil's shear strength is retained, which can offer some resistance against uplift and is therefore capable of reducing the uplift displacement of the structure. It was postulated that such lower excess pore pressures caused by the soil-structure interaction were the consequence of suppressed dilation at the crown, cyclic shearing stresses at the springing, and extensile stress or reduction in overburden stress at the invert of the floating structure (Chian and Madabhushi 2012).

Fig. 17 shows the stress state of the soil adjacent to the uplifting structure. The soil element at the springing depth of the structure experiences larger cyclic horizontal stress compared with the free field because of the relative displacement of the structure and soil. As a result, larger peak-to-peak cyclic amplitudes of the pore pressure are observed as supported by both the experimental and numerical analysis in Fig. 16. In the case of the soil element at the invert of the structure, there is a reduction in overburden pressure caused by the uplift tendency of the structure when soil liquefaction occurs as postulated by Tobita et al. (2011). As a result, low excess pore pressure is expected and confirmed in Fig. 15. This leads to a hydraulic gradient, which could have led to the displacement of soil toward the invert of underground structures as observed in earlier studies by Koseki et al. (1997), Chou et al. (2011), and Tobita et al. (2011). Because of the uplift response of the structure and large

variation of vertical stress at each half-cycle of the shaking, the peak-to-peak cyclic amplitude of the pore pressure is likely to be large. As for the soil element near the crown of the structure, it is likely to move away from the center of the structure under the suppressed upward force exerted by the uplifting structure. In addition, given the close proximity to the soil surface, there is lesser tendency for the soil near the crown to experience significant peak-to-peak pore pressure amplitude because the soil can displace vertically with the structure.

It is apparent that the general trend of excess pore-pressure generation produced by the numerical analysis matches the centrifuge results throughout the earthquake shaking, particularly at the invert and springing of the structure. In detail, the mean excess pore pressures at the invert and springing of the structure from the numerical analysis were mainly lower than those recorded in the centrifuge test, but they follow a similar trend during the shaking for 1.1D_0.22g in Fig. 14. However, the excess pore pressure at the crown differed significantly with the numerical analysis, overestimating the values obtained from the centrifuge test. The numerical analysis showed a slow build-up of excess pore pressure, whereas the centrifuge test first produced an increase in excess pore pressure before gradually decreasing after the second cycle of shaking. Such an observation indicates that the excess pore pressure was developing around the structure and led to the sharp increase in rate of uplift at the early stage of the shaking as portrayed in Fig. 10. However, as soon as the structure started displacing upward significantly, it was hampered by the resistance of the overlying soil because of suppressed dilation as it attempted to push the soil aside. As a consequence, excess pore pressures at the invert and springing were able to build up slightly higher in the centrifuge test than in the

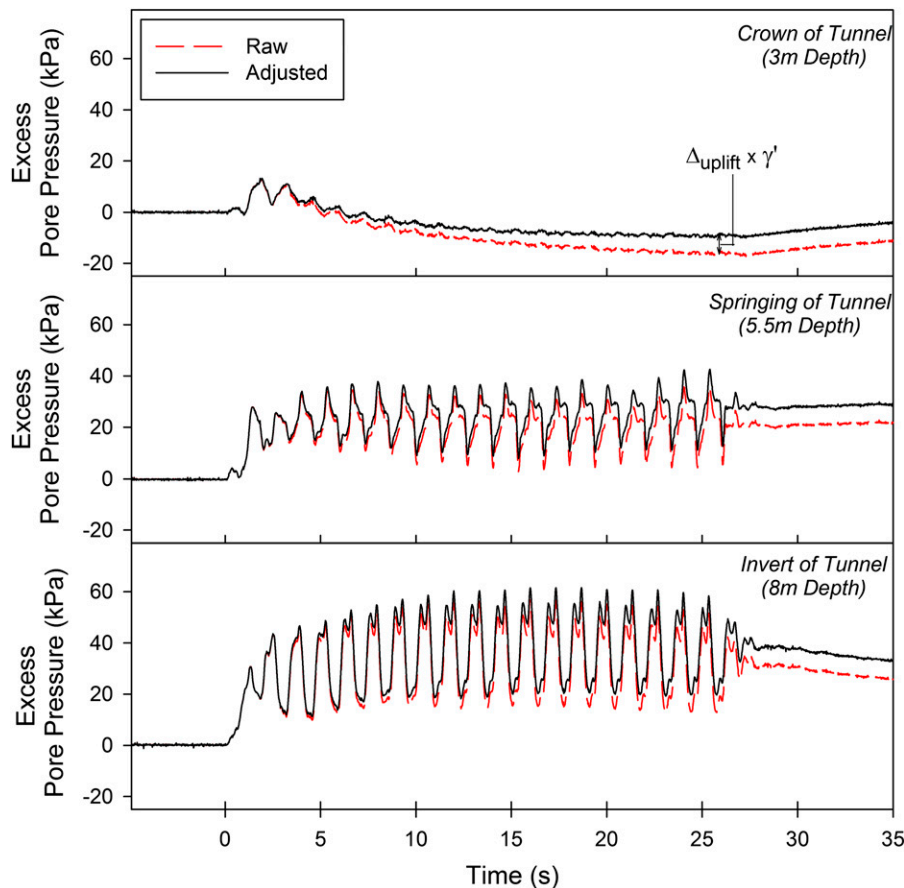


Fig. 13. Adjustment to pore pressures around structure to account for change in depth of transducers, Test 1.1D_0.22g

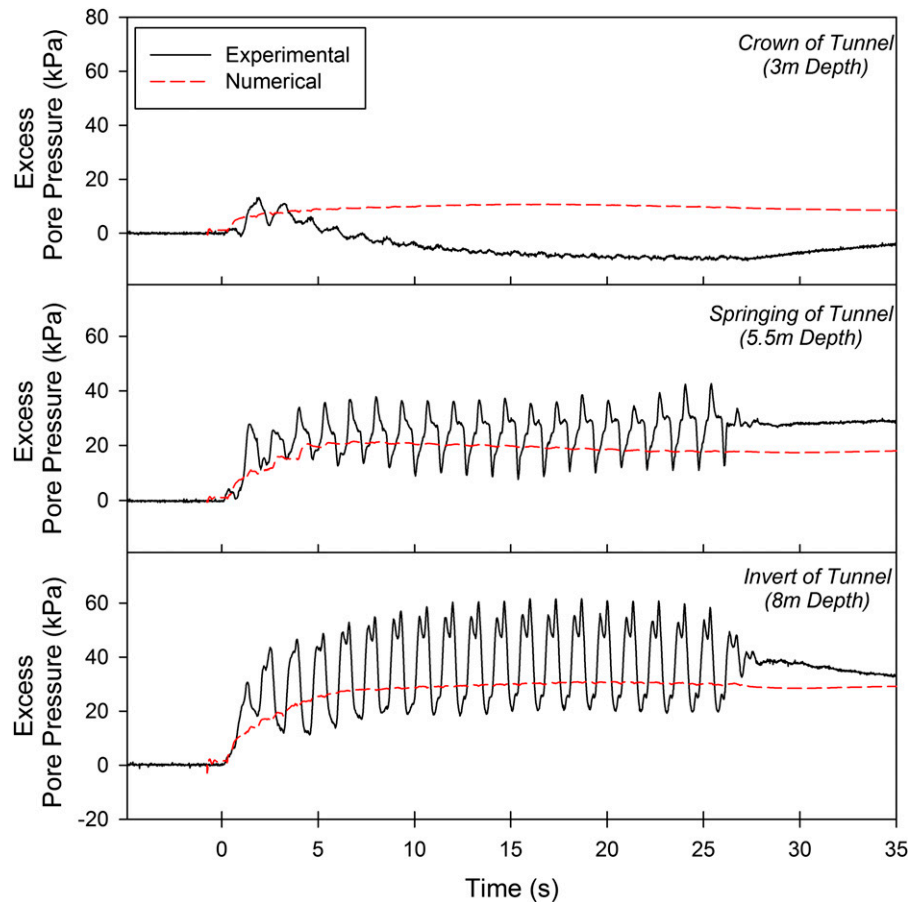


Fig. 14. Excess pore-pressure time histories around structure, Test 1.1D_0.22g

numerical analysis. These observations could have led to the differences in uplift response of the structure, especially in the early stage of the shaking as discussed previously. The delayed uplift response of the structure in the centrifuge tests also suggests the inability of the numerical analysis to capture detailed soil-structure interaction possibly because of its inherent meshing scheme.

Similar findings were also observed in the case of the deeper structure (1.5D_0.22g) in Fig. 15, except that the mean excess pore pressure at the crown was higher than the shallower structure (1.5D_0.22g) in the centrifuge test. A higher mean excess pore pressure at the crown suggests that the suppressed dilation at the overlying soil was lower. This in turn translated to a sharper rate of increase in excess pore pressure around the structure and a lower peak-to-peak variation of the excess pore pressure at the invert of the structure. The lower dilation response from the soil-structure interaction also led to a more compatible match between the numerical analysis and centrifuge test results in Fig. 15.

Soil Deformation around Buoyant Structures in Liquefiable Soil

To further evaluate the compatibility between the numerical analysis and centrifuge tests, the soil deformation around the structure was investigated. Apart from being able to replicate similar seismic wave propagation, pore-pressure generation, and structure uplift time histories as shown in previous figures, it is equally crucial that soil deformation between the two types of modeling are consistent at the same time to understand the mechanism of liquefaction-induced

uplift of underground structures. Soil deformations in the centrifuge tests with high accuracy were produced by processing large numbers of images captured with a high-speed camera through a clear window on the centrifuge strong box (window box) during earthquake shaking via a particle image velocimetry (PIV) technique (Chian and Madabhushi 2010; Cilingir and Madabhushi 2011). Soil deformation from the numerical analysis was produced using *FLAC*'s graphical user interface. Figs. 18 and 19 illustrate the spatial deformation plot produced from the centrifuge test and numerical analysis, respectively.

Based on these soil deformation plots, it is evident that the soil deformation around the structure formed wide circular loops on both sides of the structure, displacing from the crown to the invert of the structure. The overlying soil was pushed aside by the uplifting structure, whereas the region of the soil near the invert was drawn toward the expanding void beneath the structure. Given the lower excess pore pressures at the invert of the structure compared with the far field at the same depth, a hydraulic gradient exists, which induces movement of liquefied soil toward the invert of the structure because of a seepage force acting in the direction of the fluid flow. The final displacement of the soil and structure in Figs. 18 and 19 is the accumulated displacement throughout the earthquake shaking and does not represent the uplift mechanism at every juncture of the shaking. During shaking, the structure displaced both vertically and horizontally relative to the surrounding soil with each cycle of the sinusoidal shaking rather than a smooth 1D uplift movement (Chian and Madabhushi 2011). Further PIV analysis also showed the effect of densification on the uplift of the structure during the earthquake (Chian and Madabhushi 2010). These findings in the present study

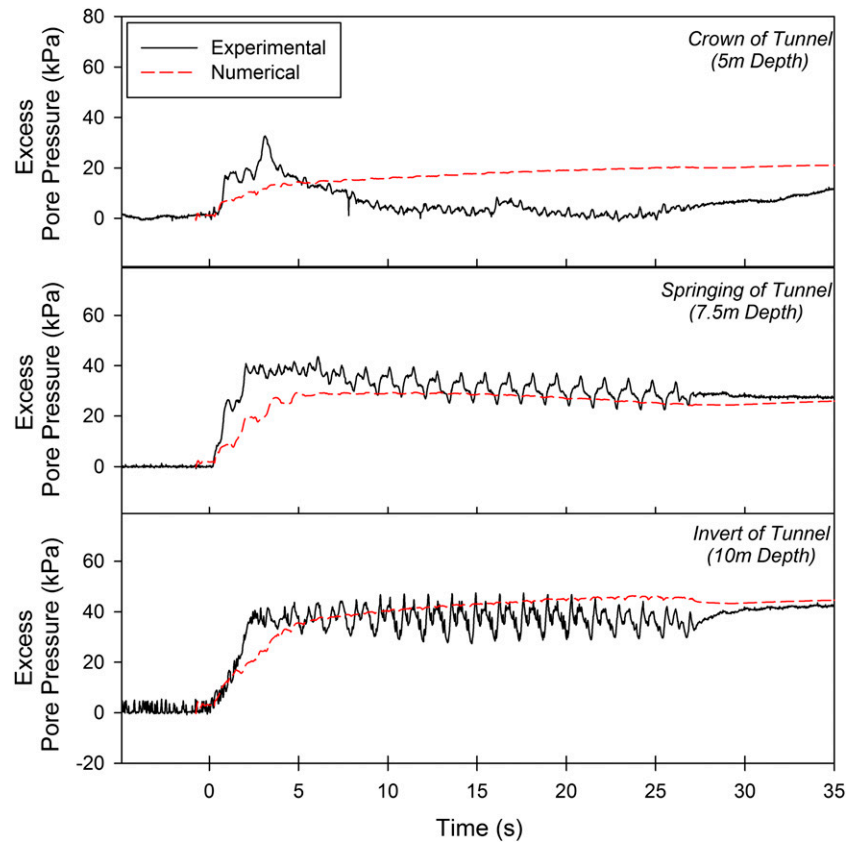


Fig. 15. Excess pore-pressure time histories around structure, Test 1.5D_0.22g

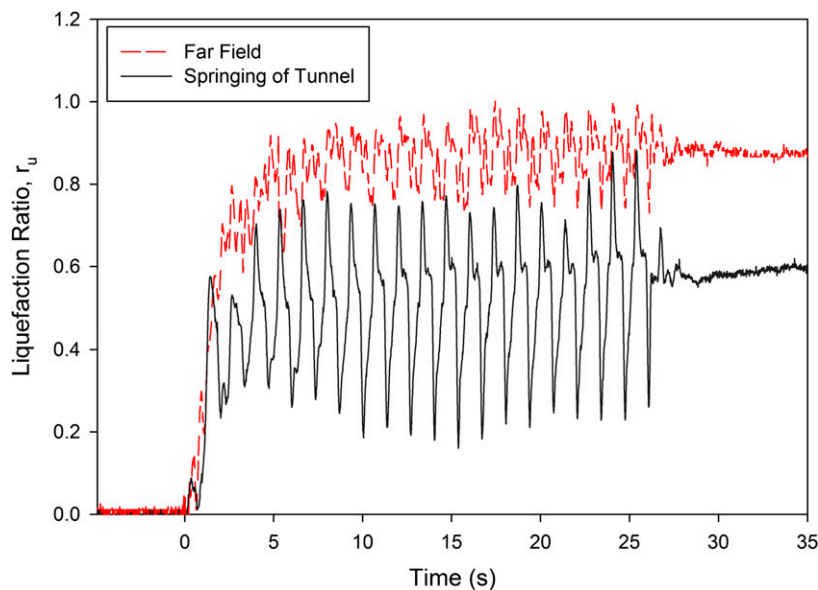


Fig. 16. Excess pore pressures at far field and springing of structure, Test 1.1D_0.22g

have undoubtedly offered a more viable means of obtaining accurate depiction and measurement of the global deformation of the liquefied soil at any instance of the shaking. The results in Figs. 18 and 19 also verified a significant amount of sand displacing toward the invert of uplifted structures as observed by earlier studies at the end of their experiments (Koseki et al. 1997; Chou et al. 2011; Tobita et al. 2011).

Numerical Simulation of Buried Sewer Pipelines in Urayasu City, Chiba Prefecture Following the 2011 Great East Japan Earthquake

Following the 2011 Great East Japan Earthquake, more than 112 manholes were uplifted, along with 28.6 km in length of damaged

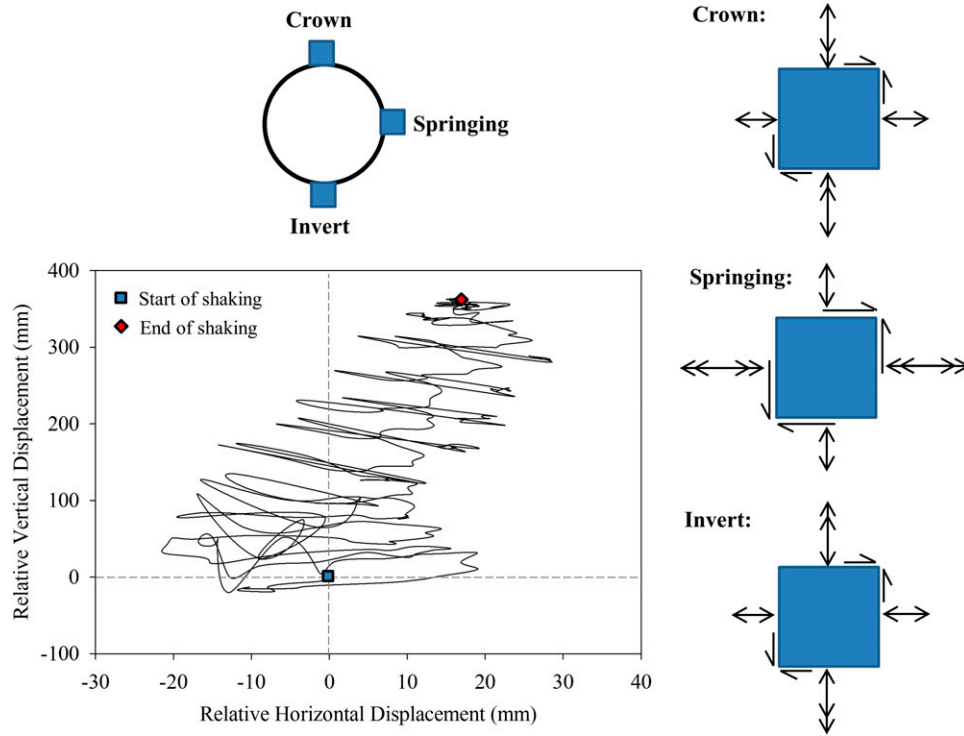


Fig. 17. Stress state of soil elements at crown, springing, and invert of structure (long shear lines and double arrowheads normal to the element indicate large stresses in that direction)

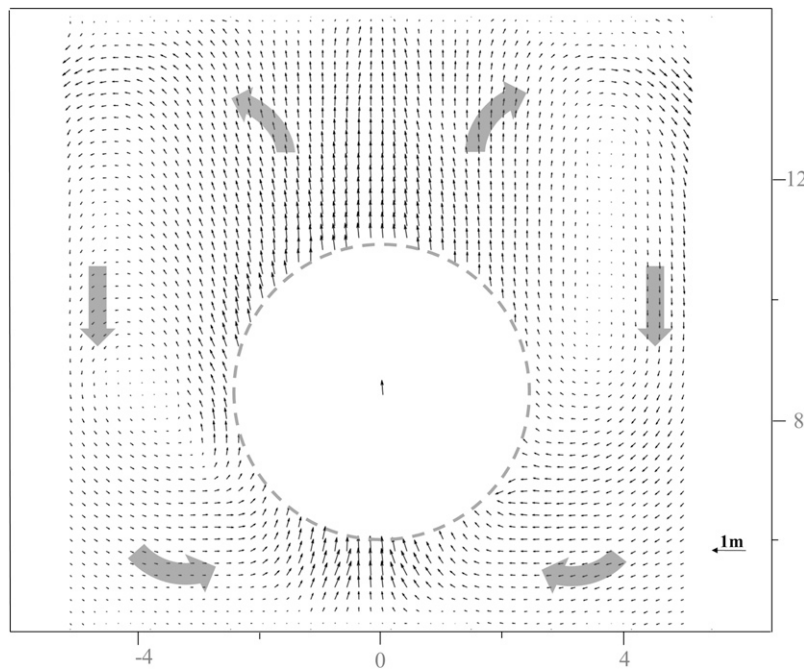


Fig. 18. Final cumulative soil deformation and displacement of structure obtained from centrifuge test, Test 1.5D_0.10g (dimensions in meters)

pipelines in Urayasu City, Chiba Prefecture near Tokyo. Fig. 20 illustrates the locations of damaged pipelines and manholes in the city. The damage was mainly located at liquefiable sites on reclaimed land, indicating the high damage susceptibility of underground structures caused by soil liquefaction. Unlike manholes, which are visible on the ground surface, the uplift of buried pipelines are less obvious. In addition, the uplift of pipes is

expected to be lower because of the presence of the overlying soil weight, higher shear resistance of the soil, and smaller displaced volume compared with its connecting manhole (Chian and Tokimatsu 2012). Despite the difficulty in measuring uplift displacement of buried pipelines in the field, the observation of several uplifted manholes (27) at Site 1 (in Fig. 20) is an obvious indirect indication of uplift of pipelines in the vicinity. In

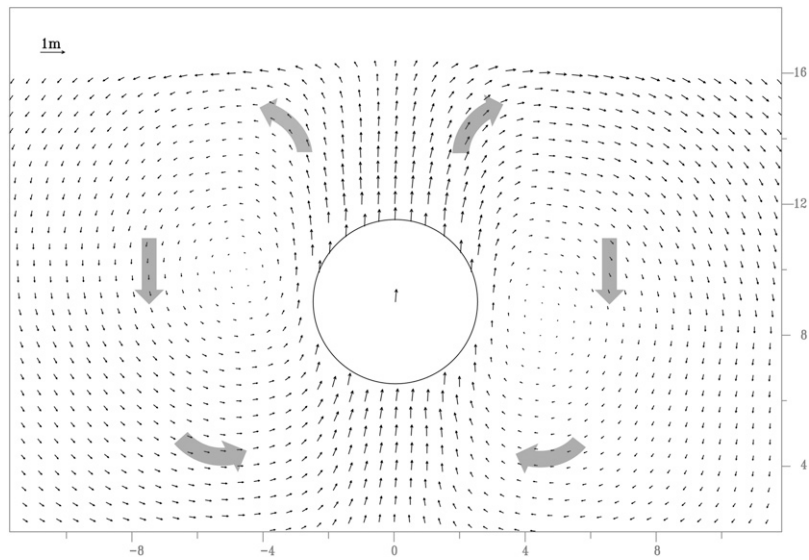


Fig. 19. Final cumulative soil deformation and displacement of structure obtained from numerical analysis, 1.5D_0.10g (dimensions in meters)

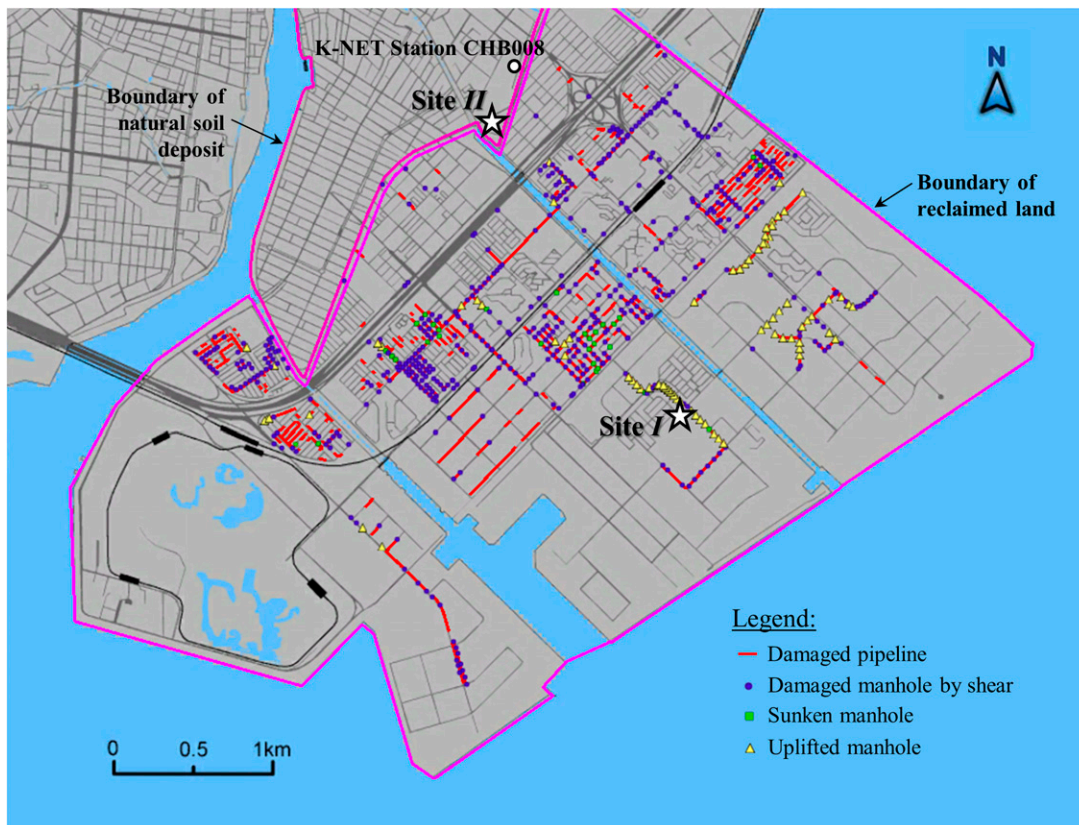


Fig. 20. Map of damaged pipelines and manholes in Urayasu City, with location of selected sites for numerical analysis (damage data from Liquefaction Mitigation Investigation Committee, Chiba Prefecture 2011)

contrast, Site II is located at the natural soil deposit, and minimal damage to manholes and pipelines were reported. Numerical simulations were conducted based on the soil profiles of Sites I and II as shown in Fig. 21. Because of the connectivity between the pipe and manhole, it is understood that the uplift of a manhole may encourage the uplift of its connecting pipeline. In view of the lack of reliable field measurements, the numerical simulations

were conducted only to provide a qualitative assessment of the uplift susceptibility of pipelines in the vicinity. The Kyoshin Network (K-NET) earthquake motion recording was first outcropped with the site condition of the K-NET station before applying to the numerical model based on the soil profile of each site. For soil layers susceptible to liquefaction, the model-specific coefficients (G_0 , h_r , k_r , and d) were calibrated from cyclic

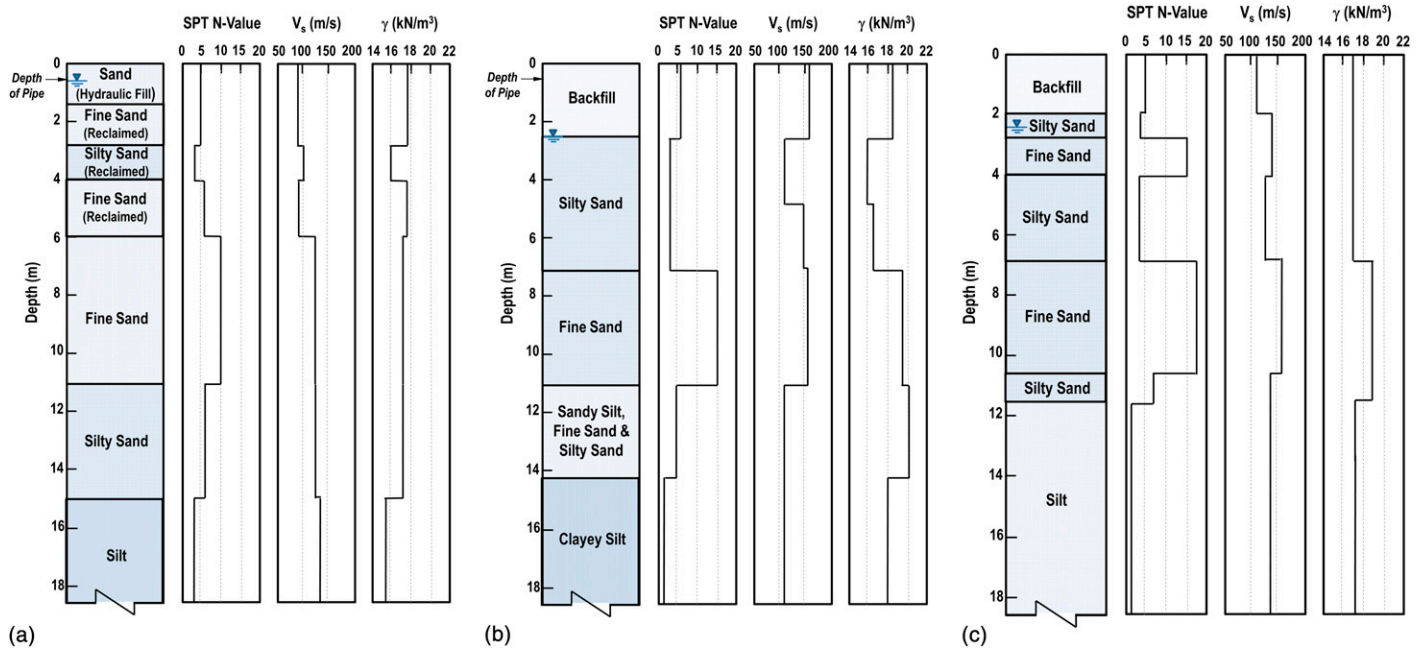


Fig. 21. Simplified soil profile at Urayasu City: (a) Site I (reclaimed land); (b) Site II (natural deposit); (c) K-NET

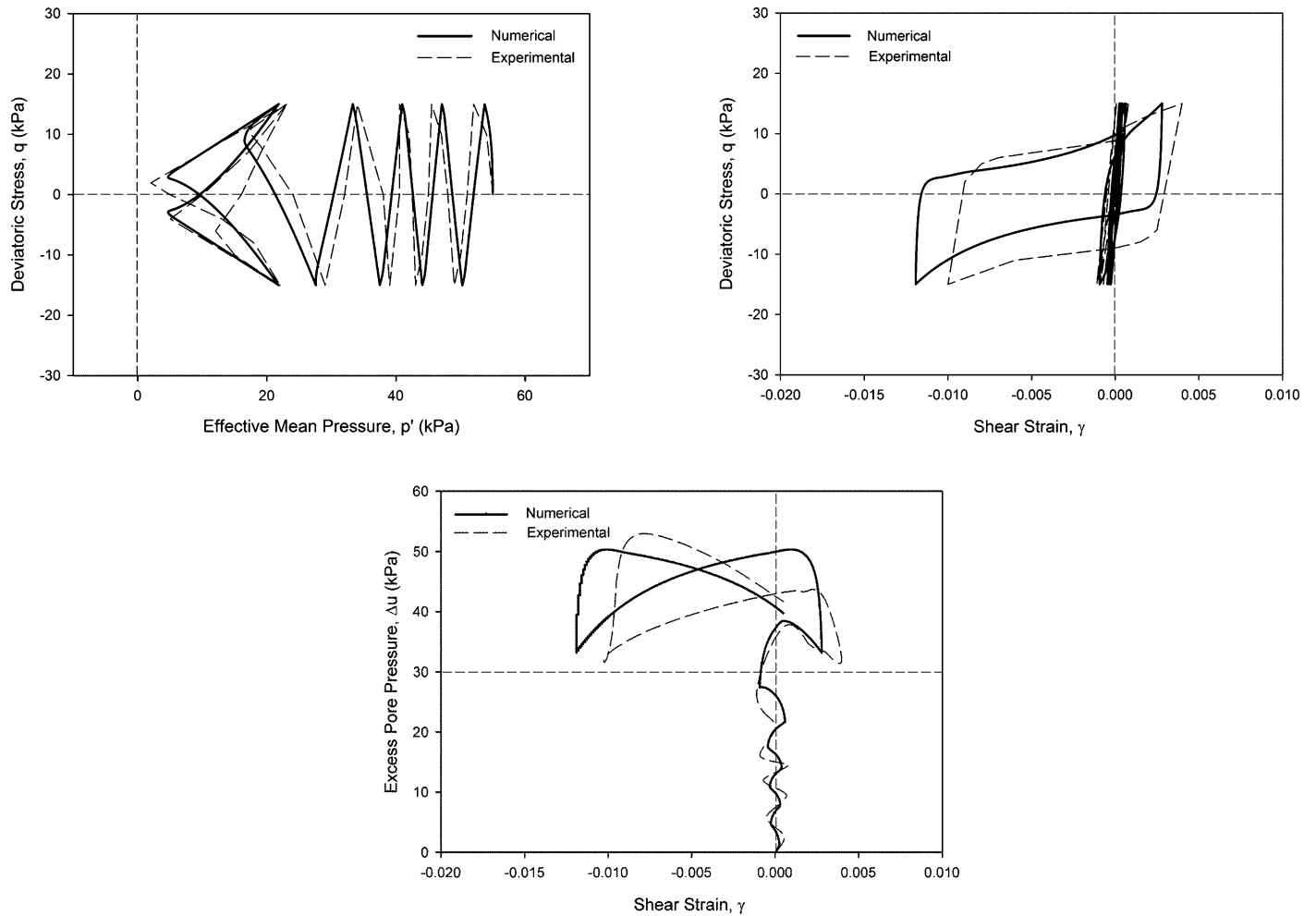


Fig. 22. Model simulation of cyclic test for Urayasu sand [experimental data from Ministry of Land, Infrastructure and Transport (MLIT) 2013]

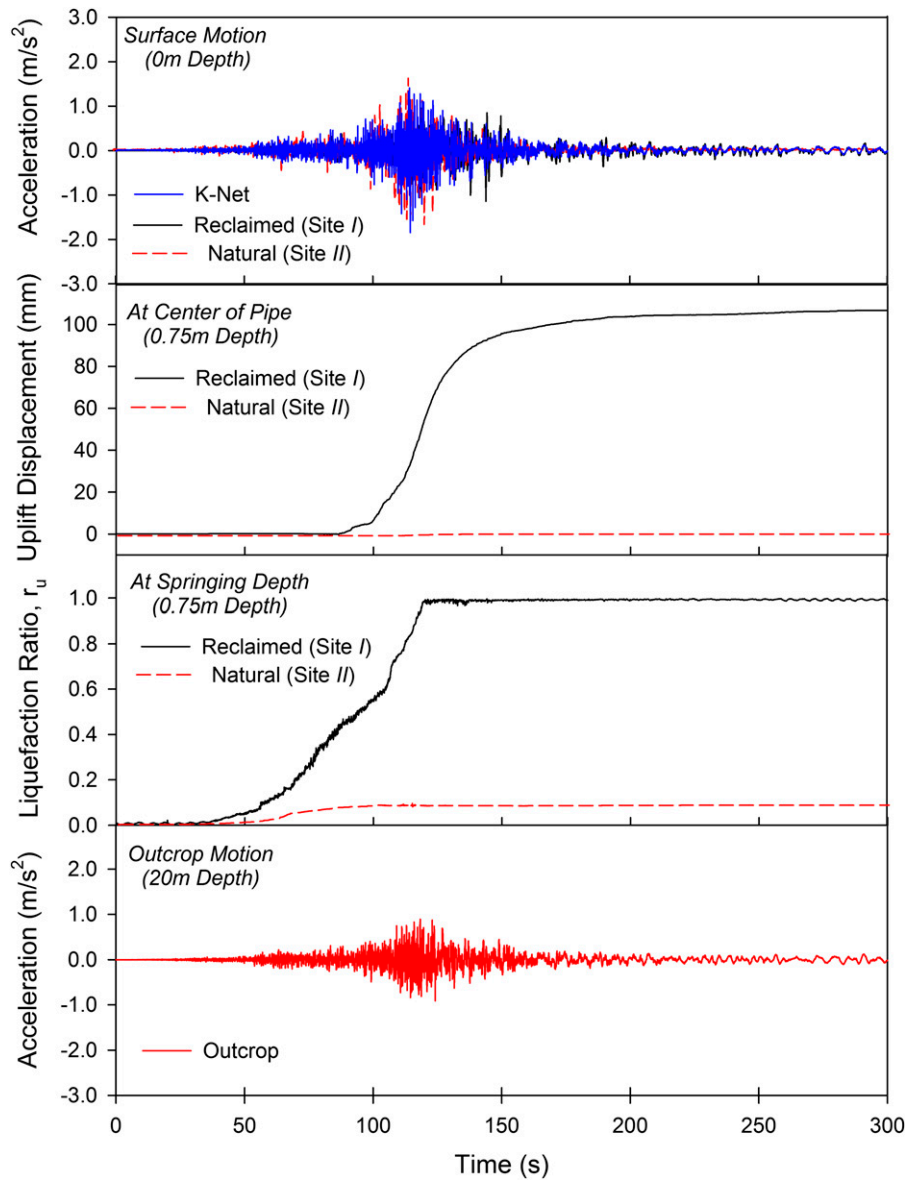


Fig. 23. Pipe uplift displacement, far-field liquefaction ratio, and input acceleration time histories

laboratory experiments of the Urayasu sand similar to the Hostun sand as shown in Fig. 22. The results of the soil and pipe responses are presented in Fig. 23.

It is evident in Fig. 23 that the uplift failure of a 300-mm-diameter pipe buried at 1.5 times its diameter (i.e., 450 mm depth) was produced in the numerical analysis at Site I, where the soil near the surface was weak given the lower standard penetration test (SPT) N -values and shear-wave velocity. In addition, a high water table at a depth of about 0.5 m was present, which encouraged soil liquefaction to occur. Such uplift of pipe can lead to cracks at the crown of the lining as supported by photographs taken by the Liquefaction Mitigation Investigation Committee of Chiba Prefecture in the field. Uplift of the pipe at Site II was minimal in the numerical analysis, which is in agreement with the field observations. Low excess pore-water pressure was produced in the analysis, which indicates retention of shear resistance of the soil and lower uplift force from the excess pore pressure at the invert of the pipe. These factors inhibit uplift of the pipe as postulated in the theoretical uplift mechanism.

Conclusion

Earthquake-induced liquefaction poses a risk of floatation of underground structures, such as tunnels and pipelines. In this paper, results from a series of numerical analyses and dynamic centrifuge tests on the uplift of shallow structures in liquefiable soils were presented. The influence of earthquake input acceleration and buried depth of the structure on its uplift response were investigated. Both numerical and experimental analyses showed comparable results in acceleration and excess pore pressure in the soil and uplift displacement of the structure. Both analyses also showed the requirement of high excess pore pressures and large input accelerations for the development of the uplift. A higher magnitude of the earthquake shaking increases the rate of uplift of the structure. In addition, the uplift of the structure ceased as soon as the shaking stopped. A higher uplift was also produced for a shallower buried structure because of the lower shear resistance and surcharge weight offered by the overlying soil. Furthermore, a constant rate of uplift was attained after the soil was liquefied, postulating a possible limit

to shear modulus degradation of the surrounding soil because of the soil-structure interaction as confirmed by lower excess pore pressures near the structure. The numerical analysis has shown to be capable of replicating the soil deformation around the structure in centrifuge tests. Further correspondence of numerical results and field observations following the 2011 Great East Japan Earthquake clearly demonstrates the prospects of applying similar numerical and/or experimental analyses for geotechnical problems associated with the floatation of underground structures in liquefiable soils.

Acknowledgments

The authors are grateful for the financial support from the Cambridge Trust at the University of Cambridge and the Japan Ministry of Education, Culture, Sports, Science and Technology via the International Urban Earthquake Engineering Center for Mitigating Seismic Mega Risk program at Tokyo Institute of Technology.

References

- Adalier, K., et al. (2003). "Centrifuge modeling for seismic retrofit design of an immersed tube tunnel." *J. Phys. Model. Geotech.*, 3(2), 23–32.
- Bouferra, R., Benseddiq, N., and Shahrou, I. (2007). "Saturation and preloading effects on the cyclic behavior of sand." *Int. J. Geomech.*, 10.1061/(ASCE)1532-3641(2007)7:5(396), 396–401.
- Byrne, P. M., et al. (2004). "Numerical modeling of dynamic centrifuge tests." *Proc., 13th World Conf. on Earthquake Engineering*, International Association for Earthquake Engineering, Tokyo.
- Cheney, J., Hor, O., Brown, R., and Dhat, N. (1988). "Foundation vibration in centrifuge models." *Proc., Centrifuge 88*, CRC Press, Rotterdam, Netherlands, 481–486.
- Chian, S. C., and Madabhushi, S. P. G. (2010). "Use of PIV analysis for soil deformations around a tunnel in liquefiable soils." *Proc., 14th European Conf. on Earthquake Engineering*, Macedonian Association for Earthquake Engineering (MAEE), Ohrid, Macedonia.
- Chian, S. C., and Madabhushi, S. P. G. (2011). "Displacement of tunnels in liquefied sand deposits." *Proc., 8th Int. Conf. on Urban Earthquake Engineering*, Center for Urban Earthquake Engineering (CUEE), Tokyo, 517–522.
- Chian, S. C., and Madabhushi, S. P. G. (2012). "Excess pore pressures around underground structures following earthquake induced liquefaction." *J. Geotech. Earthquake Eng.*, 3(2), 25–41.
- Chian, S. C., Stringer, M. E., and Madabhushi, S. P. G. (2010). "Use of automatic sand pourers for loose sand models." *Proc., 7th Int. Conf. on Physical Modelling of Geotechnics*, CRC Press, Rotterdam, Netherlands, 117–121.
- Chian, S. C., and Tokimatsu, K. (2012). "Floatation of underground structures during the M_w9.0 Tohoku Earthquake of 11th March 2011." *Proc., 15th World Conf. on Earthquake Engineering*, International Association for Earthquake Engineering, Tokyo.
- Chou, J. C., Kutter, B. L., Travararou, T., and Chacko, J. M. (2011). "Centrifuge modeling of seismically induced uplift for the BART Transbay Tube." *J. Geotech. Geoenviron. Eng.*, 10.1061/(ASCE)GT.1943-5606.0000489, 754–765.
- Cilingir, U., and Madabhushi, S. P. G. (2011). "Effect of depth on seismic response of circular tunnels." *Can. Geotech. J.*, 48(1), 117–127.
- Dafalias, Y. F., and Popov, E. P. (1977). "Cyclic loading for materials with a vanishing elastic region." *Nucl. Eng. Des.*, 41(2), 293–302.
- Fast Lagrangian Analysis of Continua (FLAC) 7* [Computer software]. Minneapolis, Itasca Consulting Group.
- Haigh, S. K., Eadington, J., and Madabhushi, S. P. G. (2012). "Permeability and stiffness of sands at very low effective stresses." *Géotechnique*, 62(1), 69–75.
- Hashiguchi, K., and Ueno, M. (1977). "Elasto-plastic constitutive laws of granular materials." *Proc., 9th Int. Conf. on Soil Mechanics and Foundation Engineering*, International Society on Soil Mechanics and Foundation Engineering, London, 73–82.
- Koseki, J., Matsuo, O., and Koga, Y. (1997). "Uplift behavior of underground structures caused by liquefaction of surrounding soil during earthquake." *Soils Found.*, 37(1), 97–108.
- Ling, H. I., Mohri, Y., Kawabata, T., Liu, H., Burke, C., and Sun, L. (2003). "Centrifugal modeling of seismic behavior of large-diameter pipe in liquefiable soil." *J. Geotech. Geoenviron. Eng.*, 10.1061/(ASCE)1090-0241(2003)129:12(1092), 1092–1101.
- Ling, H. I., Sun, L., Liu, H., Mohri, Y., and Kawabata, T. (2008). "Finite element analysis of pipe buried in saturated soil deposit subject to earthquake loading." *J. Earthquake Tsunami*, 02(01), 1–17.
- Liquefaction Mitigation Investigation Committee, Chiba Prefecture. (2011). "Reports of committee meetings on liquefaction mitigation at Urayasu, Chiba, Japan." Chiba Prefectural Government, Chiba, Japan (in Japanese).
- Madabhushi, S. P. G., Schofield, A. N., and Lesley, S. (1998). "A new stored angular momentum based earthquake actuator." *Proc., Centrifuge '98*, Vol. 1, CRC Press, Rotterdam, Netherlands, 111–116.
- Ministry of Land, Infrastructure and Transport (MLIT). (2013). "Liquefaction mitigation of residential areas using lattice-like underground wall construction method." *Technical Rep.*, Ministry of Land, Infrastructure and Transport, Tokyo (in Japanese).
- Mitrani, H. (2006). "Liquefaction remediation techniques for existing buildings." Ph.D. dissertation, Cambridge Univ., Cambridge, U.K.
- Mroz, Z., and Zienkiewicz, O. C. (1984). "Uniform formulation of constitutive equations for clays and sands." *Mechanics of engineering materials*, C. S. Desai and H. R. Gallagher, eds., Wiley, Chichester, U.K., 415–449.
- Sasaki, T., Matsuo, O., and Kondo, K. (1999). "Centrifuge model tests on uplift behavior of buried structures during earthquakes." *Proc., Int. Conf. on Earthquake Geotechnical Engineering*, Portuguese Geotechnical Society, Lisbon, Portugal, 315–320.
- Schofield, A. N. (1980). "Cambridge geotechnical centrifuge operations." *Géotechnique*, 25(4), 743–761.
- Schofield, A. N. (1981). "Dynamic and earthquake geotechnical centrifuge modeling." *Proc., Int. Conf. on Recent Advances in Geotechnical Earthquake Engineering and Soil Dynamics*, Vol. 3, Univ. of Missouri-Rolla, Rolla, MO, 1081–1100.
- Steedman, R. S., and Madabhushi, S. P. G. (1991). "Wave propagation in sand medium." *Proc., Int. Conf. on Seismic Zonation*, Earthquake Engineering Research Institute, Oakland, CA, 253–260.
- Stewart, D. P., Chen, Y.-R., and Kutter, B. L. (1998). "Experience with the use of methylcellulose as a viscous pore fluid in centrifuge models." *Geotech. Test. J.*, 21(4), 365–369.
- Stringer, M. E., and Madabhushi, S. P. G. (2009). "Novel computer-controlled saturation of dynamic centrifuge models using high viscosity fluids." *Geotech. Test. J.*, 32(6), 559–564.
- Sun, Y., Klein, S., Caulfield, J., Romero, V., and Wong, J. (2008). "Seismic analyses of the Bay Tunnel." *Proc., Int. Conf. on Geotechnical Earthquake Engineering and Soil Dynamics IV*, ASCE, Reston, VA, 1–11.
- Teymur, B. T. (2002). "Boundary effects in dynamic centrifuge modeling." Ph.D. dissertation, Cambridge Univ., Cambridge, U.K.
- Tobita, T., Kang, G.-C., and Iai, S. (2011). "Centrifuge modeling on manhole uplift in a liquefied trench." *Soils Found.*, 51(6), 1091–1102.
- Tobita, T., Kang, G.-C., and Iai, S. (2012). "Estimation of liquefaction-induced manhole uplift displacements and trench-backfill settlements." *J. Geotech. Geoenviron. Eng.*, 10.1061/(ASCE)GT.1943-5606.0000615, 491–499.
- Tokimatsu, K., Tamura, S., Suzuki, H., and Katsumata, K. (2011). "Quick report on geotechnical problems in the 2011 Tohoku Pacific Ocean Earthquake." *Technical Rep.*, Center for Urban Earthquake Engineering, Tokyo Institute of Technology, Tokyo (in Japanese).
- Wang, Z.-L., Dafalias, Y. F., and Shen, C.-K. (1990). "Bounding surface hypoplasticity model for sand." *J. Eng. Mech.*, 10.1061/(ASCE)0733-9399(1990)116:5(983), 983–1001.
- Yang, D., Naesgaard, E., Byrne, P. M., Adalier, K., and Abdoun, T. (2004). "Numerical model verification and calibration of George Massey Tunnel using centrifuge models." *Can. Geotech. J.*, 41(5), 921–942.
- Zeng, X., and Schofield, A. N. (1996). "Design and performance of an equivalent-shear-beam container for earthquake centrifuge modelling." *Géotechnique*, 46(1), 83–102.